

Point Cloud Color Constancy

Xiaoyan Xing^{1,*}, Yanlin Qian^{2,*}, Sib0 Feng², Yuhan Dong^{1,†}, and Jiri Matas³
¹Tsinghua University, ²Independent Researcher, ³Czech Technical University

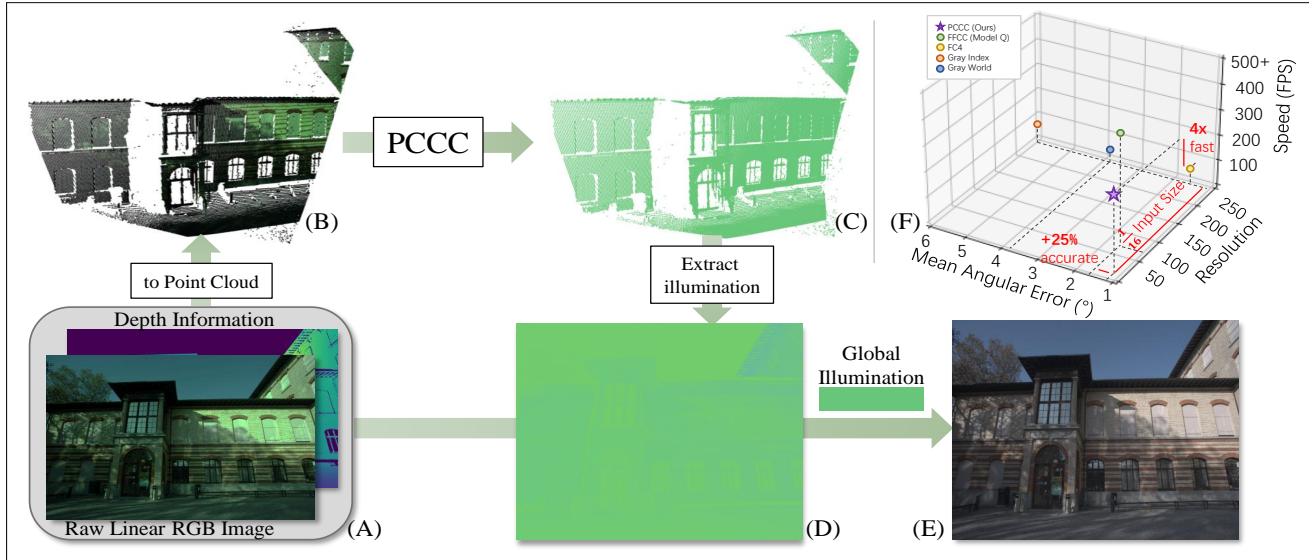


Figure 1. We present *Point Cloud Color Constancy* (PCCC), which is simple, efficient and hardware friendly. (A): Raw RGB-D image. (B): RGB point cloud generated by (A). (C): Point Cloud with illumination rendered from PCCC. (D) 2D illuminant map extracted from (C). (E) Color corrected image. (F): Speed, accuracy and parameter number comparison with state-of-the-art color constancy methods.

Abstract

In this paper, we present *Point Cloud Color Constancy*, in short *PCCC*, an illumination chromaticity estimation algorithm exploiting a point cloud. We leverage the depth information captured by the time-of-flight (ToF) sensor mounted rigidly with the RGB sensor, and form a 6D cloud where each point contains the coordinates and RGB intensities, noted as (x, y, z, r, g, b) . PCCC applies the PointNet architecture to the color constancy problem, deriving the illumination vector point-wise and then making a global decision about the global illumination chromaticity. On two popular RGB-D datasets, which we extend with illumination information, as well as on a novel benchmark, PCCC obtains lower error than the state-of-the-art algorithms. Our method is simple and fast, requiring merely 16×16 -size input and reaching speed over 140 fps (CPU time), including the cost of building the point cloud and net inference.

*Equal contribution/†Corresponding author. Code & Data: <https://github.com/xyxingx/Point-Cloud-Color-Constancy>

1. Introduction

There are over a billion smartphone cameras capturing photographs, where the procedure of perceiving true colors of the real world happens in the ISP pipeline. In general, a good-looking picture relies on a single CMOS sensor with a certain color filter array. On flagship smartphones, there is a trend of leveraging two or more digital sensors to “compute” a higher-quality image. Such cases include {main camera, tele camera} [2], {main camera, near inferred sensor} [49], and {color camera and time-of-flight (ToF) depth sensor} [46]. In this work, we proceed in this direction and use a color camera and a ToF sensor. A ToF depth sensor has been commonly employed for other applications; e.g., auto focus, bokeh effect and 3D face and skeleton scanning. Here we show a novel task based on combing the RGB and ToF sensors – RGB-D or point-cloud illumination estimation.

Illumination estimation refers to the task of estimating the normalized illumination chromaticity given a raw im-

age, which itself is a core task in computational color constancy. Color constancy is an intrinsic property of the human eye, which perceives the world independently of illumination color changes. For technical reasons and engineering benefits, in digital cameras, illumination estimation and a channel-wise rescaling are combined in the so-called auto-white balance (AWB), to realize “color constancy” computationally. An accurate estimation, with proper rescaling factors than render a neutral surface white.

In common the use-case, illumination estimation only relies on a single raw format image. Here we advocate the use of depth sensor which casts the task into a 3D regression problem, which we show delivers more accurate results. We introduce depth based color constancy for the following reasons: 1. image statistics are steered by depth information [29]. More specially, the surface geometry, the texture size and the signal-to-noise ratio varies with depth, which will influence the performance of illumination estimation algorithm; 2. abrupt depth changes correlate with non-smooth illumination distribution. Imagine walking from outside to an indoor room with a tungsten light. In a 2D image, the depth and illumination change dramatically in the area close to the door. As shown in Figure 1, the captured RGB-D images are reprojected to form the colored point cloud, on which the proposed method estimates the illumination for each point. Then these point predictions (Figure 1(C)) are averaged with learnt weights.

In a summary, the contributions of the paper are:

- We formulate the generic problem of illumination estimation in a 3D world, relaxing the over-simplistic assumptions about uniform illumination for a plain 2D image adopted in prior work .
- We present PCCC architecture, derived from PointNet, a novel point cloud net for the color constancy task. We show its superior performance on illumination estimation on three color constancy benchmarks. Side applications, *e.g.*, local AWB is reported as well.
- PCCC operates well on the sparse-sampled thumbnail point clouds, which allows over 500 frames per second (include time of building point cloud) on a Nvidia V100 GPU and is hardware friendly for a mobile SoC.
- We annotated the illumination groundtruth labels for three popular RGB-D datasets (NYU-v2 dataset [40], Diode dataset [43] and ETH3D dataset [36]) and collected DepthAWB, a novel RGB-D dataset for the color constancy task.

2. Related Work

The prior art in computational color constancy falls into the learning-based and statistics-based groups. In this section, we consider the candidate method from a different perspective, *i.e.*, the input requirement.

Methods relying on a single Image The majority of color constancy methods belong to this category. Firstly, there exist a list of traditional methods, including Gray World [12], White Patch [11], General Gray World [7], Gray Edge [42], Shades-of-Gray [21], LSRS [22], PCA [16] and Grayness Index [34], *etc.* They are easy to be implemented in a ISP chipset and may fail if their assumption is violated. Secondly, more methods are driven by the availability of color constancy datasets which provide carefully annotated illumination groundtruth; [5, 8, 13, 14, 20, 23–26, 39] learn a high-dimensional mapping from the capture raw data to the sought illumination vector after optimization on training set. The learning tools behind includes gamut mapping, least square minimization, random forest, neural networks and so on.

Methods relying on Image(s) and Auxiliary Information

There is a research trend of including more information else than a single image in design of color constancy methods, for special purposes. Abdelhamed *et al.* [2] leveraged main camera and tele camera simultaneously in a very light-weight neural network, releasing the discriminative ability of color filter array correlation. Barron *et al.* [9] proposed a Fourier transform-based model (model O in the paper), learning the model weight from the camera metadata like aperture and so on. Qian *et al.* [33, 35] claimed the preceding image sequence benefits the illumination estimation for the shot image. Yoo *et al.* [47] explored the AC light source in a high-speed setting. Ebner *et al.* [19] firstly estimated the illumination chromaticity by combing Gray World with depth map.

Differing from [19], in a end-to-end way, our approach learns how to use depth for referring illumination from a sparsely-sampled point cloud. As shown in Table ??, it also supports semantic info extraction and 3D point-wise AWB.

3. Point Cloud Color Constancy

We describe PCCC in the following order: 1) reformulating the illuminant estimation problem on RGB-D images (Section 3.1); 2) aligning the RGB images and depth maps spatially (Section 3.2); 3) generating point cloud with tristimulus color values (Section 3.3); 4) explaining our point-cloud illuminant estimation network (Section 3.4); and 5) proposing two augmentation tricks based on vibrating camera position and illumination chromaticity (Section 3.5).

3.1. Formulation

Given an RGB image \mathbf{I} , the image formation can be described as follow:

$$\mathbf{I} = \int_{\lambda} E(\lambda)S(\lambda)R_{RGB}(\lambda)d\lambda, \quad (1)$$

Spatial weighted illuminant estimation Technically, the MLP can decrease the channel of global feature \mathbf{P}_{global} from 1024 to 3, yielding the final prediction, which is simple but loses local estimates. Inspired by [25], we devise a spatially weighted estimation module, by introducing the point-cloud weight matrix \mathbf{W}_s in stage of network inferring.

To include more local information, feature extraction is boosted by aggregating the global feature \mathbf{P}_{global} and the intermediate output from first MLP group to be $\mathbf{P}_{local} \in \mathbb{R}^{N \times 1088}$. Then \mathbf{P}_{local} is reduced to $\mathbf{P}_{illums} = [\mathbf{P}_{illum}, \mathbf{W}_s] \in \mathbb{R}^{N \times 4}$ by MLP, where $\mathbf{P}_{illum} \in \mathbb{R}^{N \times 3}$ represents the illumination estimation of each point, and spatial illuminant matrix $\mathbf{W}_s \in \mathbb{R}^{N \times 1}$. Mathematically global illuminant $\hat{\mathbf{E}}_{global} \in \mathbb{R}^{1 \times 3}$ can be achieved by :

$$\hat{\mathbf{E}}_{global} = \sum_{R,G,B} (\text{softmax}(\mathbf{W}_s) \cdot \mathbf{P}_{illum}), \quad (4)$$

where softmax normalizes \mathbf{W}_s into $\{0,1\}$ as a probability mask. The global illuminant is employed for global color constancy. The probability mask and local illuminant can later be leveraged for the trial in local AWB.

Loss Function Similar to the prior arts, we use the recovery angular loss \mathcal{L}_{ang} as our loss function:

$$\mathcal{L}_{ang}(\hat{\mathbf{E}}, \mathbf{E}) = \arccos\left(\frac{\hat{\mathbf{E}} \cdot \mathbf{E}}{\|\hat{\mathbf{E}}\| \cdot \|\mathbf{E}\|}\right), \quad (5)$$

where $\hat{\mathbf{E}}$ is the predicted illumination vector and \mathbf{E} is the ground truth illumination label. With the loss, our net converges in an end-to-end way.

Discussion Theoretically, any network that design for point clouds [28, 32] or for RGB-D input can be employed to replace the PointNet-based net here. However, due to the nature of the color constancy problem, we argue that an ideal point cloud color constancy network should 1) have a simple but effective structure that keeps good trade-off between accuracy and running speed; 2) be not sensitive to the noise and sparse sampling rate and 3) in default working with thumbnail-size input, which is usually provide by specialized ISP hardware node. Quantitative experiments to the mentioned properties of our design are in Section 5.3.

3.5. Point Cloud Augmentation

Point cloud allows us to augment data from a 3D perspective. We propose two augmentation methods based on our observation that illumination on a point is roughly invariant to mild *camera pose* jittering and *light intensity* changes. These methods rely on separating a point cloud into two parts 1) coordination value \mathbf{P}_{xyz} and 2) color value \mathbf{P}_{RGB} , considering the order of point cloud is fixed during our augmentation period. We can augment the camera position and light intensity separately as following.

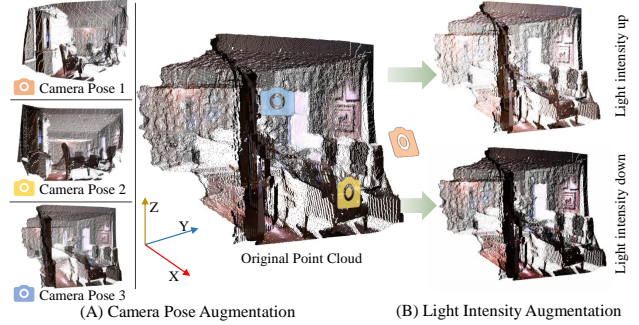


Figure 3. We use two augmentation approaches: (A) camera pose augmentation simulates images capture from a different viewing angle. (B) light intensity augmentation generates new pixel-wise illumination field under the same illuminant.

Camera Pose Augmentation is inspired by that small rotation does not affect the decision of the dominant illumination color. As shown in Figure 3, we sample a rotation matrix $\mathbf{R} \in SO(3)$ to simulate the scenarios where we take images from different perspectives.

Light Intensity Augmentation is inspired by luminance can be changed when the relative distance of the illuminated objects and the light source changes. Based on this, we use an intensity scaling factor L to realize luminance-based augmentation.

Considering both augmentation ways, the new point cloud \mathbf{P}' is:

$$\mathbf{P}' = \mathbf{R}\mathbf{P}_{xyz} \oplus L\mathbf{P}_{RGB}, \quad (6)$$

where \mathbf{R} is the sampled rotation matrix, L is a scalar from a normal distribution $\mathcal{N}(1, 0.15^2)$, and \oplus is channel-wise concatenation.

4. Dataset Preparation

To train PCCC, the pairs of the point sets (from RGB-D images) and the corresponding illumination labels are needed. However, to our knowledge, there are no such datasets publicly available. To evaluate our method, we first present in Section 4.1 reannotating the commonly used depth datasets NYU-v2 [40] and Diode [43]. Then in Section 4.2 we relabel the ETH3D dataset [36], which includes sensor raw files. Finally and the most importantly, we show the collection of our point cloud illumination dataset using a single lens digital camera and an accompanied Intel laser depth sensor.

4.1. Annotating NYU-v2 & Diode Depth Dataset

NYU-v2 [40] is a classical RGB-D dataset, with hundreds of indoor scenes captured by Microsoft Kinect. Diode [43] is a latest RGB-D dataset released by Toyota Technological Institute at Chicago, this dataset contains more

than 20 scenes include indoor and outdoor scenes. Affected by the illuminant and position, there are numbers of AWB-biased images in these datasets (See supplement material). We found these images are suitable for us to label the correct illumination according to the neutral surfaces and validate the color constancy algorithm.

Images from these two datasets are in sRGB. To label the ground truth illuminant, we process images by the following steps: 1) switch sRGB to LRGB using inverse gamma operation [6, 18]; 2) remove the tuning operation using a 3×3 matrix as suggested in [3]; and 3) label out the neutral surface area (which is deemed as neutral without doubt, like white printed paper) and calculate the illumination vector (Details in supplement materials). The steps can be formulated as:

$$\mathbf{E}_{label} = \Gamma(\mathbf{M}^{-1} \times \mathbf{I}_{sRGB}^{1/\gamma}), \quad (7)$$

where $\Gamma(\cdot)$ represents the area selection and illuminant calculation. \mathbf{E}_{label} is the labeled ground truth illumination, \mathbf{M} is the tuning matrix of images.

After the preprocessing steps, we obtain linearization images with labels from two datasets. These images contain indoor and outdoor scenes, with diverse label distribution.

Discussion We acknowledge that relabeled illumination on sRGB images may not be as accurate as that in raw LRGB images, and our transformation can not really transform the sRGB to LRGB, which is a rough operation and may bring noise to the images. Since all color constancy methods will suffer the same bias on the datasets, we argue that these data are of experimental value for us to test our method (See Section 5 for more experimental details).

4.2. Annotating ETH3D Depth Dataset

ETH3D dataset [36] is a stereo RGB-D dataset with 13 different scenes with indoor and outdoor, the RGB images are captured by a Nikon D3 camera, and the depth maps are from a radar. The dataset provides the raw format of images. We can process the images using LibRaw, and obtain the raw linear RGB images, which makes them closer to the images we used in camera auto white balance pipeline.

We use the similar label method as Section 4.1 to obtain the illuminant. Considering we already have raw DSLR images \mathbf{I}_{Raw} , the labeled illuminant \mathbf{E}_{label} can be obtained by:

$$\mathbf{E}_{label} = \Gamma(\mathbf{I}_{Raw}). \quad (8)$$

4.3. DepthAWB – Real Color Constancy Dataset with Depth

Despite we have the annotated dataset on raw images, still the ground truth illuminants have biases, since we can not really know the accurate color. Therefore, an RGB-D dataset with raw images and color checker labeled illuminants is needed. Following prior works on RGB-D

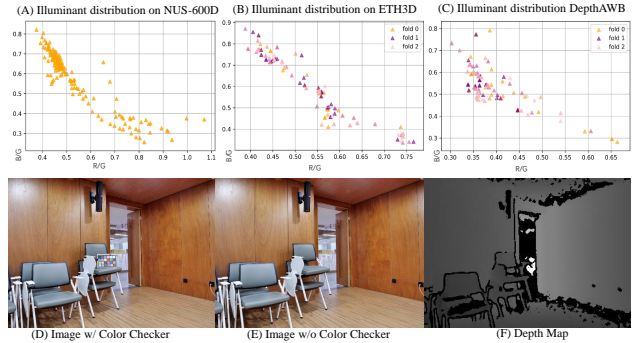


Figure 4. (A)-(C): Illumination distribution of NUS-600D dataset, our relabel ETH3D dataset and propose dataset. (D), (E) a pair of images we captured sequentially. We use (D) with color checker for labelling and (E) for training and testing. (F) ToF depth map.

datasets collection [40] and color constancy dataset collection [23], we collected our own depthAWB dataset, which to our knowledge is the first RGB-D dataset with labeled illuminant. Our dataset preparation steps are as following:

Data collection: Since RGB-D camera like Kinect-V2 does not provide the raw images, therefore, following [36], we use LUMIX GH5S camera¹ to capture the DSLR RGB images and Intel Resense L515 to capture the depth maps. Our data capture setup is presented in supplement material.

Data calibration: Calibration is a fundamental operation, as introduced in Section 3.2, we first capture several images from RGB camera and depth camera, by tilting the a checker board with checker size 30 millimeter vertically and horizontally; then we calculate the transformation matrix using the Caltech camera calibration toolbox [1].

Illuminant annotation: Since we obtain the raw images in data collection, we demosaic the raw images similar as Section 4.2, and we directly annotated the ground truth on the xrite color checkerboard.

4.4. Illumination distribution

In Figure 4 (A)-(C), we compare the illumination distribution of our labeled ETH3D dataset, our collected Depth AWB dataset to the commonly used NUS dataset [16] Canon 600D subset (NUS-600D). Our datasets cover a wide range of illuminant values, and share the same trend in illuminant distribution as NUS-600D.

5. Experiments

We evaluate PCCC and a large list of prior methods on three public RGB-D datasets (relabeld by us, Section 4.1 and 4.2) and a newly-collected RGB-D dataset (Section 4.3). The dataset overview is as follows:

¹We fixed focal length and set camera aperture as $f/8.0$, while extend the shutter speed, details discussed in supplement.

Method	Angular Error (NYUv2&Diode)					Angular Error (ETH3d RAW)					Angular Error (DepthAWB)					Training time (s) ¹	Test time (ms)
	Mean	Med.	Tri.	B25%	W25%	Mean	Med.	Tri.	B25%	W25%	Mean	Med.	Tri.	B25%	W25%		
GrayWorld [12]	5.39	3.83	4.37	1.23	11.81	3.18	2.87	2.95	1.00	5.70	6.03	5.23	5.40	3.48	9.75	-	10.00
WhitePatch [11]	6.37	5.53	5.59	3.77	10.46	6.28	6.41	6.49	1.20	13.09	11.77	12.51	12.23	3.74	18.80	-	7.83
1 st GrayEdge [42]	4.02	2.71	2.96	0.82	9.43	7.81	5.44	6.49	1.06	17.09	6.56	6.13	6.06	1.52	12.83	-	34.00
2 nd GrayEdge [42]	4.15	2.90	3.10	0.78	9.81	8.02	5.30	6.38	1.21	18.20	7.12	6.91	6.97	1.87	13.07	-	42.50
Shade of Gray [21]	3.69	2.68	2.90	0.61	8.59	7.25	5.02	6.23	0.95	15.59	5.84	4.59	5.11	1.22	11.82	-	320.00
APAP (GW) [4]	3.47	2.31	2.61	0.67	7.78	2.71	2.53	2.54	0.82	4.69	3.69	2.69	3.08	1.70	6.50	16	16.00
Shen et al. [37]	5.55	3.61	3.88	1.03	13.39	3.90	3.12	3.31	1.08	7.54	5.05	3.19	3.80	0.77	11.85	-	37.00
GI [34]	4.28	3.01	3.27	0.85	9.81	3.26	2.02	2.19	0.49	7.35	3.91	2.09	2.58	0.49	10.23	-	109.00
Bayesian [23]	9.64	10.01	9.59	3.61	15.68	7.32	5.31	6.02	1.70	15.42	5.97	5.09	5.24	1.91	11.20	35	2134.42
Cheng et al. [17]	3.11	2.02	2.27	0.59	7.39	3.44	1.71	2.06	0.44	9.43	1.89	1.15	1.24	0.22	4.71	63	331.20
Quasi U CC [10]	3.76	2.20	2.54	0.45	9.28	3.90	3.29	3.43	0.85	7.58	4.45	3.80	3.90	1.04	9.03	-	345.13
FC4 [25]	2.49	1.61	1.79	0.47	6.03	1.19	0.90	0.98	0.32	2.46	1.34	0.98	1.04	0.24	3.08	13000	38.21
FFCC (Model J) [9]	2.82	1.87	2.00	0.51	6.82	1.16	0.91	0.99	0.31	2.43	1.32	0.76	0.88	0.27	3.21	67	29.00
FFCC (Model Q) [9]	2.75	1.90	2.01	0.48	6.63	1.08	0.88	0.91	0.26	2.26	1.40	0.81	0.93	0.29	3.40	51	1.10
Ours (16 Points, w/o depth)	2.96	1.82	2.12	0.63	6.91	1.58	0.98	1.09	0.22	3.82	2.60	2.11	2.20	0.50	5.72	1700	4.00
Ours (16 Points)	2.23	1.67	1.74	0.40	5.16	1.12	0.75	0.78	0.14	2.79	1.64	0.95	1.05	0.17	4.30	1700	4.00
Ours (256 Points, w/o depth)	2.80	1.89	2.22	0.57	6.39	1.42	1.02	1.08	0.33	3.11	2.39	1.75	1.90	0.42	5.50	3120	7.03
Ours (256 Points)	2.20	1.42	1.58	0.34	5.30	0.88	0.53	0.62	0.17	2.15	1.05	0.37	0.55	0.09	3.02	3120	7.03
Ours (4096 Points)	2.18	1.30	1.54	0.33	5.39	0.78	0.42	0.51	0.11	1.97	0.99	0.28	0.50	0.08	2.94	5700	47.12

¹ Since we have multi-scale datasets, the train time is for the DepthAWB dataset.

² The profiled time for PCCC includes the time slot for aligning RGB image and depth image, building point cloud and also network inferring.

Table 1. Quantivate comparison of our reannotated NYU-v2 [40], Diode [43], ETH3D [36] datasets and our collected dataset, respectively. We highlight top two performers in each metric with pink and yellow background, respectively. All test time are CPU time.

BackBone	Image Scale	Train time	FPS	NYUv2&Diode				ETH3d RAW				DepthAWB			
				Mean	Med.	Tri.	W25%	Mean	Med.	Tri.	W25%	Mean	Med.	Tri.	W25%
PointCNN [28]	16*16	~ 2	~ 20	2.41	1.68	1.83	5.58	1.55	1.33	1.35	3.09	2.59	1.78	1.95	5.92
PointCNN [28]	64*64	> 24	~ 5	2.19	1.55	1.69	5.02	1.30	1.02	1.11	2.72	1.31	0.91	0.97	3.00
PointNet++ [32]	16*16	~ 3	~ 100	2.69	2.87	3.76	3.59	1.44	1.50	1.52	1.93	1.61	1.56	1.57	2.39
PointNet++ [32]	64*64	> 24	~ 3	2.98	1.98	2.20	7.04	1.66	1.25	1.34	3.39	1.91	2.02	1.99	2.57
Ours	16*16	~ 0.5	~ 530	2.35	1.58	1.80	5.37	1.08	0.78	0.87	2.43	1.05	0.37	0.55	3.02
Ours	64*64	~ 1.5	~ 495	2.20	1.30	1.57	5.53	0.87	0.52	0.61	2.13	0.99	0.28	0.50	2.94

Table 2. Quantitative results of point cloud based backbones. We test three different backbones on three datasets, with two different input scales respectively. Training time in hours. FPS is from GPU. Color setting as in Table 1.

- **NYU-v2 & Diode Dataset:** 324 linearized RGB images and their corresponding depth map from NYU-v2 [40] and Diode datasets [43].
- **ETH3D Dataset:** 195 reprocessed Raw RGB images and their corresponding depth map from ETH-3D datasets [36].
- **DepthAWB Dataset:** 185 DSLR RGB images captured by LUMIX GH5S and depth maps by Intel Realsense L515.

Training: We use Pytorch to build and train our method on NVIDIA V100 (Tesla) GPU, Adam [27] is employed as the optimizer. The learning rate is 0.0003. The epoch is set to 10k.

Metrics: Similar as prior color constancy tasks [44, 45, 48], we report the mean, median (Med.), trimean (Tri.), best (B) and worst (W) 25% of angular error (Equation (5)). To validate our method’s time efficiency, we also present the time cost during training (for the learning-based methods) and testing (for all).

5.1. Quantitative Results

Table 1 presents the quantitative results of PCCC and a large selection of prior arts on three RGB-D color constancy datasets. In overall, the proposed PCCC (with 4096 points) leads three leaderboards, obtaining the lowest error in almost all statistics. Shrinking the input size to 256 points², PCCC also performs steadily better than the state-of-the-art learning based methods [9, 25] by a large margin, again showing the advantage of PCCC. To our a bit surprise, the PCCC model with 16-points input still delivers meaningful results, demonstrating the net learns the illumination from the 96 float values w.r.t. image.

From a multiview point of view, 3D point cloud can be rendered to 2D images, as done in [31], which forms a projection-based augmentation boosting the task performance.

It worth mentioning that all PCCC variants provide an over-realtime inference time, nearly 7 mini-seconds (equals to 140 frames per second) on CPU. Considering the tiny input size, we believe it is a viable solution for smartphone

²This equals to a 16×16 RGB image plus a same-size depth map.

Module			Angular Error (16x16)				Angular Error (64x64)			
CPA	LIA	SW	Mean	Med	Tri.	W25%	Mean	Med	Tri.	W25%
-	-	-	1.32	0.81	0.90	3.35	1.33	0.75	0.90	3.61
-	-	✓	1.23	0.79	0.88	3.14	1.18	0.53	0.70	3.19
-	✓	✓	1.14	0.57	0.72	3.13	1.04	0.43	0.60	2.95
✓	-	✓	1.19	0.50	0.72	3.32	1.10	0.42	0.63	3.16
✓	✓	✓	1.05	0.37	0.55	3.02	0.99	0.28	0.50	2.94

Table 3. PCCC ablation study. On the DepthAWB dataset, for we two resolutions of the point cloud – 16x16 (left) and 64x64 (right). CPA - camera pose augmentation, LIA - light intensity augmentation; both described in Section 3.5. SW - refers to the spatial weighting, see Section 3.4. Color setting as in Table 1.

photography.

Figure 6 shows a qualitative comparison of PCCC and our selected well-performing methods. Among all choices, the proposed method obtains the lowest error and delivers the most neural appearance, for both outdoor and indoor scenarios. Please see supplement for more visual results.

Notice All learning-based methods and their hyper-parameters are from their official implementations or carefully tuned. All test time are the CPU time.

5.2. What Depth Brings

In Table 1, we also report the results when PCCC is not given depth (in practice, it is done by initializing the depth as 1 uniformly). We observe that, for 16-points and 256-points models, the accuracy degenerates by a noticeable gap, proving the contribution of the depth. On ETH3d and DepthAWB datasets, the PCCC variant without depth still performs over the majority of learning-based methods, showing that it learns to infer illumination chromaticity well from a “flatten” point cloud. Empirically, we deduce that depth itself contains color information but provides geometric clue for PCCC to tell how the illumination varies from one location to another in a 3D space.

Figure 5 visualizes the illumination certainty map to evaluate the importance of depth information. With depth, PCCC can aggregate feature more from the area which is of more “achromatic” surface and meaningful depth.

5.3. Ablation Study

Point Cloud Processing Backbone As discussed in Section 3.4, there are obviously many selections for point cloud based net that can be employed as the backbone of the proposed method. We replace the PointNet backbone by different point cloud nets (e.g., PointCNN [28], PointNet++ [32]) and test their performance in our task.

Table 2 proves that given the input of same size, PointNet backbone gives better mean angular error compared to PointCNN and PointNet++ backbones, while costs much less time ($\sim 1/80$ times). As PointNet backbone achieves a good trade-off between accuracy and efficiency, we adopt

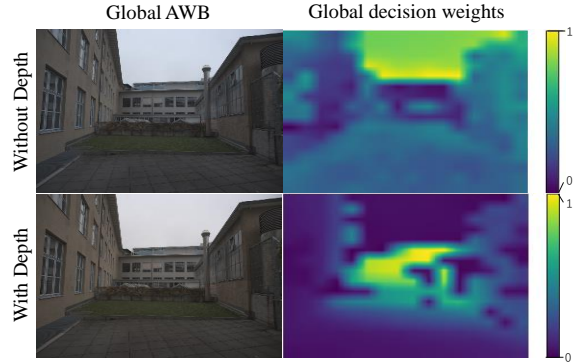


Figure 5. Illustration of how the depth affects the final decision. Depth information helps PCCC to estimate illumination from more meaningful information (building wall) instead of noisy information (bright sky with disturbing color).

PointNet as our default backbone. For fair comparison, only the backbone is switched while other modules are the same.

Point Set Size and Augmentation We investigate the influence of three proposed modules: camera pose augmentation (CPA), light intensity augmentation (LIA), and spatial weight distribution (SW), using two different size point clouds 16×16 and 64×64 respectively.

Results are shown in Table 3. Compared to using a very sparsely-sampled point cloud (256 points), the 4096-point point cloud obtains better results on each metric. By deactivating each devised module (CPA, LIA, SW) one by one, we notice a gradual performance drop, which validates the benefit of each module.

5.4. Beyond Global Illumination Estimation

Considering that in PCCC illumination-related feature is deduced point-wisely, it is straight-forward to explore its potential application in point-wise AWB (or referred as local AWB).

As introduced in Section 3.4, we can achieve point-wise illumination distribution (later weighted by a weight matrix and fused into the global illuminant). If we take this intermediate feature as our final output, we obtain a $N \times 3$ illumination tensor, where N is the point number. The illumination tensor can be visualized as a colored point cloud (Figure 7, 2nd row), and, if projected to pixel coordinate system, as a 2D illumination map (Figure 7, 3rd row).

With 2D illumination map, getting the reciprocals for each point’s vector yields its AWB gain. We apply the AWB gain pixelwisely and visualize in Figure 8. Comparing the image intensities recovered by both solutions, we can find the local one more accurately estimate the dual illumination.

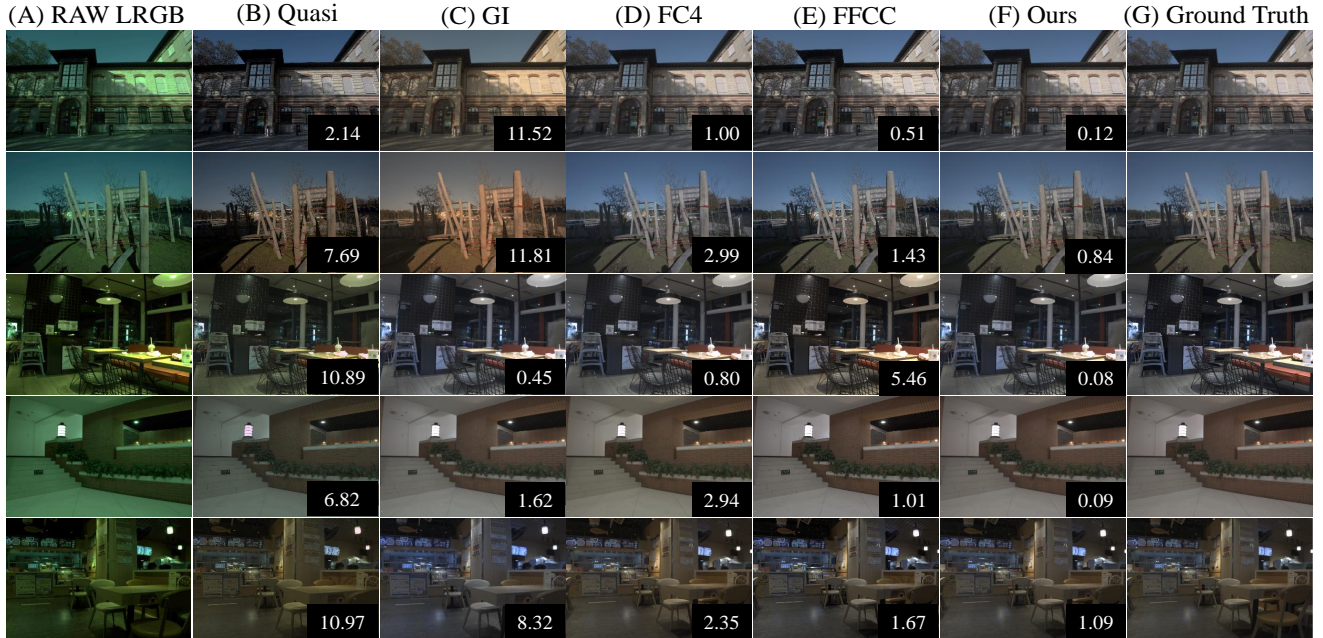


Figure 6. Quantitative global illuminant estimation results on the relabeled ETH3d dataset [36] and the new DepthAWB dataset. (A) and (G) are Raw linear RGB images and images corrected by ground truth illuminants, respectively. From (B) to (F): images with estimated illuminants from Quasi [10], Gray Index [34], FC4 [25], FFCC [9], and PCCC, respectively.

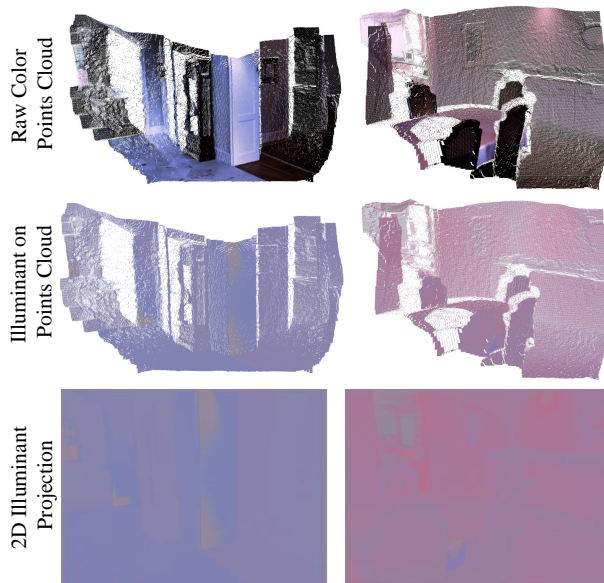


Figure 7. Illustration of illumination distribution over 3D point clouds and the corresponding 2D illumination maps.

6. Conclusion

We develop a point set-based regression net, PCCC, for the color constancy task. By leveraging the geometry information and extensive point-wise augmentation, it deduces the global illumination chromaticity accurately, even

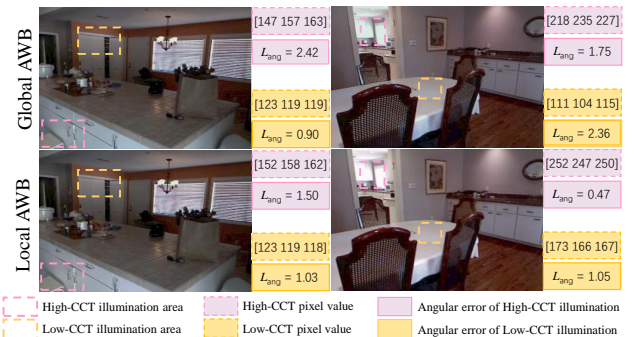


Figure 8. Visualization of Global AWB result and Local AWB result. We use yellow and cyan bounding box to indicate the lower and higher correlated color temperature (CCT), respectively.

in challenging mixed-lighting environments. On two popular RGB-D datasets which we added illumination information to, and on the novel DepthAWB benchmark, PCCC obtains lower error than over the state-of-the-art, reaching the mean angular error equals of 0.99 degree on DepthAWB. Its side applications like local AWB is also discussed. The PCCC method is efficient, using just 16×16 -size input, and fast, reaching ~ 140 fps on CPU. In future work, we would like to study more specific point cloud-based operator for color processing task and its interpretability.

Limitations: The quality and quantity of datasets can be further improved, including add Local AWB labels.



Figure 9. AWB-biased images and their corrected version with our labeled ground-truth illuminations from DIODE datasets [43] and NYU-v2 [40], respectively.

A. Dataset Preprocessing

Introduced in paper Section 4, we use three public RGBD datasets and collect DepthAWB dataset for point cloud color constancy. We will detail the procedure of labeling the datasets and collecting our dataset.

A.1. Incorrect White Balance

In camera ISP auto white balance (AWB) is a fundamental processing step, where the incorrect white balance images may exist due to fragile AWB algorithm or improper manual setting. Figure 9 shows the AWB-biased samples we found in the NYU-v2 dataset [40] and DIODE dataset [43], these images are linearized sRGB image.

A.2. Public Datasets Labeling

Cheng *et al.* [15] identified 66 images with two illuminations from Gehler-Shi dataset [23, 38], and relabeled two illumination vectors by finding neutral objects in the scene. We use the same idea to label the dominant illumination for NYU-v2 [40], DIODE [43] and ETH3d [36] datasets. Given a raw image \mathbf{I} , we first locate several areas under the cast of the dominant light, e.g. a piece of printed paper under the sunlight outside the window, and a gray wall illuminated by the ceiling light in the room. Then we visually check whether the area is saturated or underexposed, and select the well-exposed part. As the final step we average the rgb intensities of the selected area \mathbf{I}_{sel} , yielding the global illumination \mathbf{E} :

$$\mathbf{E} = \frac{1}{N} \sum_{R,G,B} \mathbf{I}_{sel}. \quad (9)$$

Figure 10 shows the resulting corrected images if we label correctly or with some mistake.

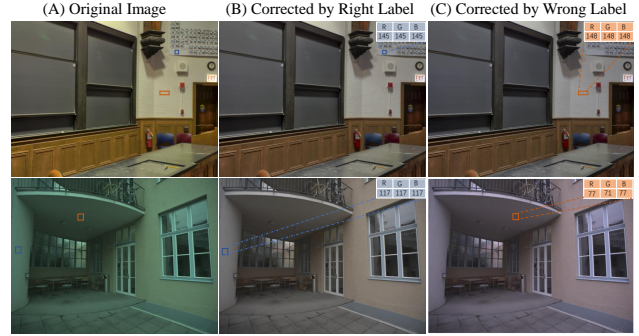


Figure 10. Illustration of the procedure of labeling the illumination by finding canonical neutral surface. We mark the blue and red boxes in column (A) indicating the right and wrong area of ground truth illumination calculation, respectively. Column (B) presents images corrected with right label. Column (C) shows images with wrong label. $\gamma = 2.2$ is applied for visualization.



Figure 11. Selected scenes from DepthAWB dataset

A.3. Dataset Collection

Our DepthAWB dataset contains of three types data, 1) RGB images by GH5s camera, 2) depth maps by Intel Realsense L515 LiDAR camera, and 3) illumination ground-truth by labeling from Xrite Color Checker.

Images from our dataset are mainly collected under indoor scenarios, considering the following reasons: 1) limited working range of the depth camera, similar as NYU-v2 [40] and SUN RGB-D [41], and 2) comparing to the outdoor scenarios, the indoor scenes have more artificial and mixed illumination which makes the illumination estimation more challenging.

We collect our data in several different places to ensure diverse scenes and wide illumination distribution. We are interested in challenging scenes, e.g., shopping mall, large pure color area, and the scene containing illumination-like misleading color. We also pay attention to areas under mixed-illumination but have one dominant illumination. Figure 11 shows several selected scenes from our dataset.

Our data capture setup is shown in Figure 12, the Intel Realsense L515 depth camera is set on the top of Panasonic



Figure 12. Our data capture setup.

Lumix GH5s camera.

We fix the camera focal length during shooting, the camera aperture is set as $f/8.0$, and we use aperture priority mode to yield a clear vision and less noise. RGB camera is placed on a tripod and ToF camera keeps the rigid connection with RGB camera.

We create a script to collect RGB images and depth maps from two cameras simultaneously, with a single click on the laptop keyboard.

A reliable illumination label lays on putting the color checker in the right position. In each scene, we put the color checker under the dominant illumination, and make sure the color checker reflects the dominant illumination into the camera. For the similar scenes under same dominant illumination, we direct use the first labeled illumination. We took two images at one single scene, one image with color checker is for the illumination labeling, and another without color checker is for the training and testing period.

We obtain the ground-truth illumination using the right exposed grayscale color on color checker.

A.4. Illumination Distribution

Theoretically, computational color constancy is to learn a mapping pattern from images in wild to illumination in wild. Therefore, a fair and complete illumination distribution is needed. We compare our collection and relabeled datasets to two widely used color constancy datasets on illumination distribution. Figure 4. in main paper shows the illumination distribution of each datasets, similar as the NUS-600D color constancy datasets, the illumination distribution of our datasets are also following the blackbody radiation curve. And Our datasets contain a relatively large range of illumination.

B. Camera Calibration

We present the camera intrinsics we used or calibrated in three different datasets.

B.1. DepthAWB Dataset

DepthAWB dataset RGB camera (Under (480,640)):

$$\begin{bmatrix} 464.0010 & 0 & 319.4235 \\ 0 & 463.1813 & 241.4676 \\ 0 & 0 & 1 \end{bmatrix} \quad (10)$$

DepthAWB dataset RGB camera (Under (240,320)):

$$\begin{bmatrix} 232.1495 & 0 & 157.8825 \\ 0 & 232.0269 & 123.0501 \\ 0 & 0 & 1 \end{bmatrix} \quad (11)$$

DepthAWB dataset Depth camera (Under (480,640)):

$$\begin{bmatrix} 470.2773 & 0 & 295.0742 \\ 0 & 470.2187 & 242.5917 \\ 0 & 0 & 1 \end{bmatrix} \quad (12)$$

DepthAWB dataset Depth camera (Under (240,320)):

$$\begin{bmatrix} 233.5576 & 0 & 148.4298 \\ 0 & 233.6542 & 125.9854 \\ 0 & 0 & 1 \end{bmatrix} \quad (13)$$

Rotation:

$$\begin{bmatrix} 0.9999 & 0.0096 & -0.0103 \\ -0.0097 & 0.9999 & -0.0063 \\ 0.0102 & 0.0064 & 0.9999 \end{bmatrix} \quad (14)$$

Shift:

$$\begin{bmatrix} 0.8710 & -105.6946 & -90.1409 \end{bmatrix} \quad (15)$$

B.2. NYU-v2 Dataset

NYU dataset RGB camera (Under (480,640)):

$$\begin{bmatrix} 525.0 & 0 & 319.5 \\ 0 & 525.0 & 329.5 \\ 0 & 0 & 1 \end{bmatrix} \quad (16)$$

B.3. DIODE Dataset

DIODE dataset RGB camera (Under (480,640)):

$$\begin{bmatrix} 866.81 & 0 & 512.0 \\ 0 & 927.06 & 384.0 \\ 0 & 0 & 1 \end{bmatrix} \quad (17)$$

B.4. ETH3D Dataset

ETH3D presents different RGB camera intrinsics on different scene, where we only use a common setting in our point cloud building, since we only need the relative distance between pixels.

ETH3D dataset RGB camera (Under (4032,6048)):

$$\begin{bmatrix} 3406.79 & 0 & 3040.861 \\ 0 & 3404.57 & 2014.4 \\ 0 & 0 & 1 \end{bmatrix} \quad (18)$$

C. More Visual Results

We present the visual results of global and local illumination estimation.

C.1. Global Illumination Estimation

We show more visual comparison results with two state-of-the-art color constancy methods in Figure 13. As introduced in Section 5 of main paper, our PCCC performs well in majority scenes, yet it also has some limitation in solving huge gray-like area (row 1&2 of Figure 13). Our method outperforms other methods on other scenes, including, dominating pure-color surface (row 3-5 of Figure 13).

C.2. Local Illumination Estimation

Unlike thumbnail size point clouds we used in global illumination estimation task, we feed full-scale point cloud to the learned PCCC to obtain higher resolution illumination map.

Pixel-wise illumination correction results are achieved by the pixel-wise map and presented in Figure 14. We select the multi-illuminant scenes from our DepthAWB dataset and NYU-v2 dataset [40]. The second row of Figure 14 shows images recovered by the illumination map. In column 1, our method corrected the illuminations from outside and the windows, separately. In column 4, our method also recovered the outdoor illumination, while keeping the indoor light the same.

References

- [1] Camera calibration toolbox. http://www.vision.caltech.edu/bouquetj/calib_doc/, Accessible at 30/10/2021. 5
- [2] A. Abdelhamed, A. Punnappurath, and M. S. Brown. Leveraging the availability of two cameras for illuminant estimation. In *CVPR*, pages 6637–6646, 2021. 1, 2
- [3] M. Afifi, B. Price, S. Cohen, and M. S. Brown. When color constancy goes wrong: Correcting improperly white-balanced images. In *CVPR*, pages 1535–1544, 2019. 5
- [4] M. Afifi, A. Punnappurath, G. Finlayson, and M. S. Brown. As-projective-as-possible bias correction for illumination estimation algorithms. *JOSA A*, 36(1):71–78, 2019. 6
- [5] A. Gijssenij, T. Gevers, and J. Van De Weijer. Generalized gamut mapping using image derivative structures for color constancy. *Springer IJCV*, 86(2-3), 2010. 2
- [6] M. Anderson, R. Motta, S. Chandrasekar, and M. Stokes. Proposal for a standard default color space for the internet—srgb. In *CIC*, volume 1996, pages 238–245. Society for Imaging Science and Technology, 1996. 5
- [7] K. Barnard, V. Cardei, and B. Funt. A comparison of computational color constancy algorithms. i: Methodology and experiments with synthesized data. *TIP*, 11(9), 2002. 2
- [8] J. T. Barron. Convolutional color constancy. In *ICCV*, 2015. 2
- [9] J. T. Barron and Y.-T. Tsai. Fast fourier color constancy. In *CVPR*, 2017. 2, 6, 8, 12
- [10] S. Bianco and C. Cusano. Quasi-unsupervised color constancy. In *CVPR*, pages 12212–12221, 2019. 6, 8
- [11] D. H. Brainard and B. A. Wandell. Analysis of the retinex theory of color vision. *JOSA A*, 3(10), 1986. 2, 6
- [12] G. Buchsbaum. A spatial processor model for object colour perception. *Journal of the Franklin Institute*, 310(1), 1980. 2, 6
- [13] A. Chakrabarti. Color constancy by learning to predict chromaticity from luminance. In *NIPS*, 2015. 2
- [14] A. Chakrabarti, K. Hirakawa, and T. Zickler. Color constancy with spatio-spectral statistics. *IEEE TPAMI*, 34(8), 2012. 2
- [15] D. Cheng, A. Kamel, B. Price, S. Cohen, and M. S. Brown. Two illuminant estimation and user correction preference. In *CVPR*, 2016. 9
- [16] D. Cheng, D. K. Prasad, and M. S. Brown. Illuminant estimation for color constancy: Why spatial-domain methods work and the role of the color distribution. *JOSA A*, 31(5):1049–1058, 2014. 2, 5
- [17] D. Cheng, B. Price, S. Cohen, and M. S. Brown. Effective learning-based illuminant estimation using simple features. In *CVPR*, 2015. 6
- [18] M. Ebner. *Color constancy*, volume 7. John Wiley & Sons, 2007. 5
- [19] M. Ebner and J. Hansen. Improving color constancy in the presence of multiple illuminants using depth information. In *International Conference on Bio-inspired Systems and Signal Processing*, volume 2, pages 133–140. SCITEPRESS, 2014. 2, 3
- [20] G. D. Finlayson. Corrected-moment illuminant estimation. In *ICCV*, 2013. 2
- [21] G. D. Finlayson and E. Trezzi. Shades of gray and colour constancy. In *Color Imaging Conference (CIC)*, 2004. 2, 6
- [22] S. Gao, W. Han, K. Yang, C. Li, and Y. Li. Efficient color constancy with local surface reflectance statistics. In *ECCV*, 2014. 2
- [23] P. V. Gehler, C. Rother, A. Blake, T. Minka, and T. Sharp. Bayesian color constancy revisited. In *CVPR*, 2008. 2, 5, 6, 9
- [24] A. Gijssenij and T. Gevers. Color constancy using natural image statistics and scene semantics. *IEEE TPAMI*, 33(4), 2011. 2
- [25] Y. Hu, B. Wang, and S. Lin. FC4: Fully convolutional color constancy with confidence-weighted pooling. In *CVPR*, 2017. 2, 4, 6, 8, 12
- [26] H. R. V. Joze and M. S. Drew. Exemplar-based color constancy and multiple illumination. *IEEE TPAMI*, 36(5), 2014. 2
- [27] D. P. Kingma and J. Ba. Adam: A method for stochastic optimization. *arXiv preprint arXiv:1412.6980*, 2014. 6
- [28] Y. Li, R. Bu, M. Sun, W. Wu, X. Di, and B. Chen. Pointcnn: Convolution on x-transformed points. *Advances in neural information processing systems*, 31:820–830, 2018. 4, 6, 7
- [29] R. Lu, A. Gijssenij, T. Gevers, V. Nedović, D. Xu, and J.-M. Geusebroek. Color constancy using 3d scene geometry. In *ICCV*, pages 1749–1756, 2009. 2, 3

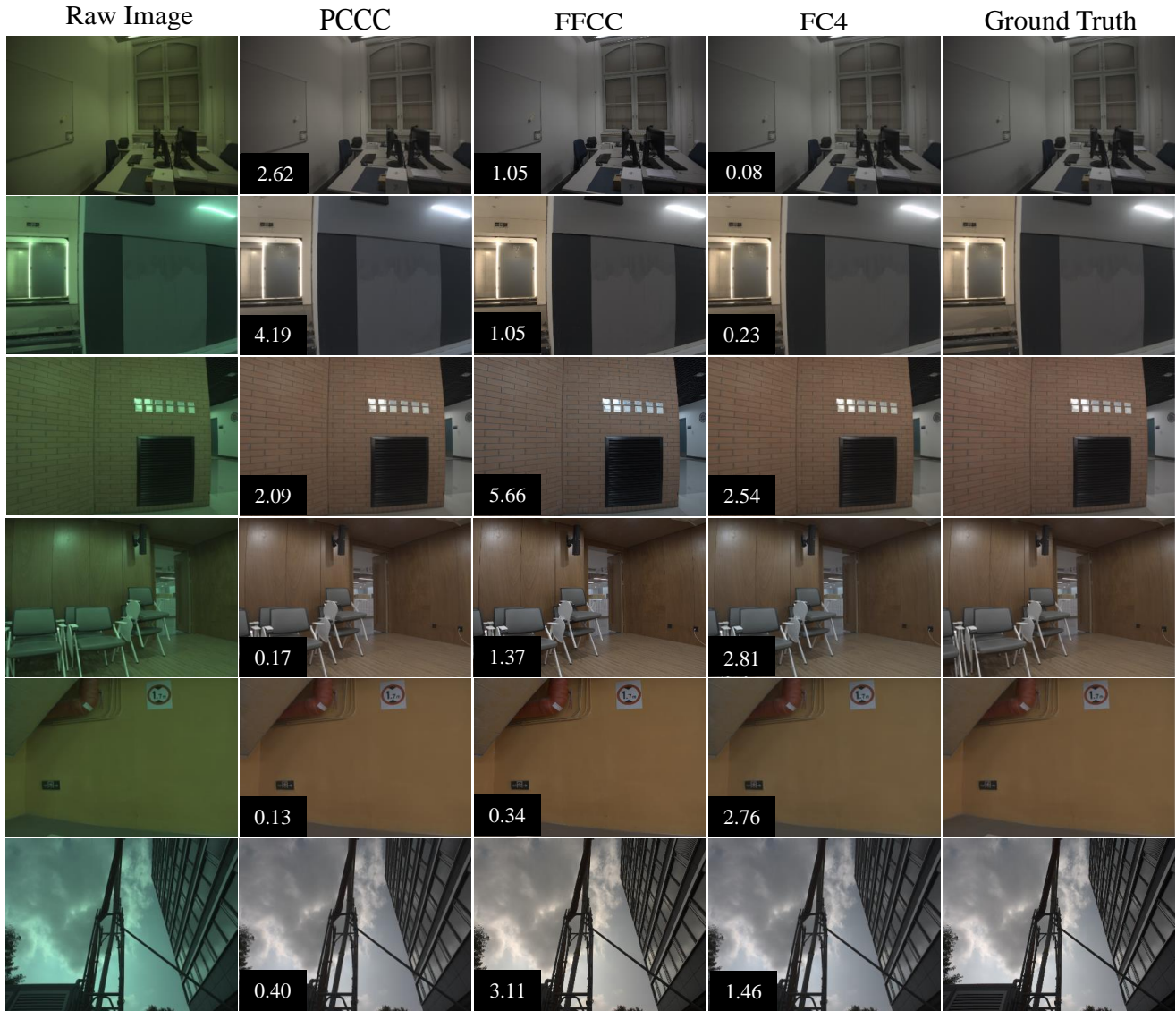


Figure 13. More visual results of our methods comparing with FC4 [25] and FFCC [9]. The angular error of each image is listed in the black box. We present our failure (angular error > 2) and well (angular error < 0.5) estimation results.

- [30] C. R. Qi, H. Su, K. Mo, and L. J. Guibas. Pointnet: Deep learning on point sets for 3d classification and segmentation. In *CVPR*, pages 652–660, 2017. 3
- [31] C. R. Qi, H. Su, M. Nießner, A. Dai, M. Yan, and L. J. Guibas. Volumetric and multi-view cnns for object classification on 3d data. In *CVPR*, pages 5648–5656, 2016. 6
- [32] C. R. Qi, L. Yi, H. Su, and L. J. Guibas. Pointnet++: Deep hierarchical feature learning on point sets in a metric space. *Advances in Neural Information Processing Systems*, 30, 2017. 4, 6, 7
- [33] Y. Qian, K. Chen, J. Kämäräinen, J. Nikkanen, and J. Matas. Recurrent color constancy. In *ICCV*, 2017. 2
- [34] Y. Qian, J.-K. Kamarainen, J. Nikkanen, and J. Matas. On finding gray pixels. In *CVPR*, 2019. 2, 6, 8
- [35] Y. Qian, J. Käpylä, J.-K. Kämäräinen, S. Koskinen, and J. Matas. A benchmark for burst color constancy. In *EC-CVW*, 2020. 2
- [36] T. Schps, J. L. Schnberger, S. Galliani, T. Sattler, and A. Geiger. A multi-view stereo benchmark with high-resolution images and multi-camera videos. In *CVPR*, 2017. 2, 4, 5, 6, 8, 9
- [37] H.-L. Shen and Q.-Y. Cai. Simple and efficient method for specular removal in an image. *Applied optics*, 48(14):2711–2719, 2009. 6
- [38] L. Shi and B. Funt. Re-processed version of the gehler color constancy dataset of 568 images. accessed from <http://www.cs.sfu.ca/~colour/data/>, 2010. 9
- [39] W. Shi, C. C. Loy, and X. Tang. Deep specialized network



Figure 14. More visual results of our methods on pixel-wise illumination estimation, we select dual-illuminant scenes from DepthAWB and NYU-v2 datasets, the first row is the original images, and the second row shows images recovered by our pixel-wise illumination map.

for illumination estimation. In *ECCV*, 2016. 2

- [40] N. Silberman, D. Hoiem, P. Kohli, and R. Fergus. Indoor segmentation and support inference from rgb-d images. In *ECCV*, pages 746–760. Springer, 2012. 2, 4, 5, 6, 9, 11
- [41] S. Song, S. P. Lichtenberg, and J. Xiao. Sun rgb-d: A rgb-d scene understanding benchmark suite. In *CVPR*, pages 567–576, 2015. 9
- [42] J. Van De Weijer, T. Gevers, and A. Gijsenij. Edge-based color constancy. *IEEE TIP*, 16(9), 2007. 2, 6
- [43] I. Vasiljevic, N. Kolkin, S. Zhang, R. Luo, H. Wang, F. Z. Dai, A. F. Daniele, M. Mostajabi, S. Basart, M. R. Walter, et al. Diode: A dense indoor and outdoor depth dataset. *arXiv preprint arXiv:1908.00463*, 2019. 2, 4, 6, 9
- [44] J. Xiao, S. Gu, and L. Zhang. Multi-domain learning for accurate and few-shot color constancy. In *CVPR*, 2020. 6
- [45] B. Xu, J. Liu, X. Hou, B. Liu, and G. Qiu. End-to-end illuminant estimation based on deep metric learning. In *CVPR*, 2020. 6
- [46] S. Yan, J. Yang, J. Kapyla, F. Zheng, A. Leonardis, and J.-K. Kamarainen. Depthtrack: Unveiling the power of rgb-d tracking. In *ICCV*, pages 10725–10733, 2021. 1
- [47] J.-S. Yoo and J.-O. Kim. Dichromatic model based temporal color constancy for ac light sources. In *CVPR*, 2019. 2
- [48] H. Yu, K. Chen, K. Wang, Y. Qian, Z. Zhang, and K. Jia. Cascading convolutional color constancy. In *AAAI*, 2020. 6
- [49] X. Zhang, T. Sim, and X. Miao. Enhancing photographs with near infrared images. In *CVPR*. IEEE, 2008. 1
- [50] Z. Zhang. A flexible new technique for camera calibration. *IEEE TPAMI*, 22(11):1330–1334, 2000. 3